



Approximate Riemann solver for the two-fluid plasma model [☆]

U. Shumlak ^{*}, J. Loverich

University of Washington, Aerospace and Energetics Research Program, Seattle, WA 98195-2250, USA

Received 8 August 2002; received in revised form 14 February 2003; accepted 24 February 2003

Abstract

An algorithm is presented for the simulation of plasma dynamics using the two-fluid plasma model. The two-fluid plasma model is more general than the magnetohydrodynamic (MHD) model often used for plasma dynamic simulations. The two-fluid equations are derived in divergence form and an approximate Riemann solver is developed to compute the fluxes of the electron and ion fluids at the computational cell interfaces and an upwind characteristic-based solver to compute the electromagnetic fields. The source terms that couple the fluids and fields are treated implicitly to relax the stiffness. The algorithm is validated with the coplanar Riemann problem, Langmuir plasma oscillations, and the electromagnetic shock problem that has been simulated with the MHD plasma model. A numerical dispersion relation is also presented that demonstrates agreement with analytical plasma waves.

© 2003 Elsevier Science B.V. All rights reserved.

Keywords: Plasma; Two-fluid; Approximate Riemann

1. Introduction

Plasmas may be most accurately modeled using kinetic theory where the plasma is described by distribution functions in physical space, velocity space, and time, $f(\mathbf{x}, \mathbf{v}, t)$. The evolution of the plasma is then modeled by the Boltzmann equation

$$\frac{\partial f_\alpha}{\partial t} + \mathbf{v}_\alpha \cdot \frac{\partial f_\alpha}{\partial \mathbf{x}} + \frac{q_\alpha}{m_\alpha} (\mathbf{E} + \mathbf{v}_\alpha \times \mathbf{B}) \cdot \frac{\partial f_\alpha}{\partial \mathbf{v}} = \frac{\partial f_\alpha}{\partial t} \Big|_{\text{collisions}} \quad (1)$$

for each plasma species $\alpha =$ ions, electrons. The Boltzmann equation coupled with Maxwell's equations for electromagnetic fields completely describe the plasma dynamics. Algorithms have been developed which model plasmas using the Boltzmann equation with specific forms of the collision operator (Vlasov equation and Fokker–Planck equation) [1–6]. However, the Boltzmann equation is seven-dimensional. As a

[☆] Supported by AFOSR Grant No. F49620-02-1-0129.

^{*} Corresponding author.

E-mail address: shumlak@aa.washington.edu (U. Shumlak).

consequence of the large dimensionality plasmas are simulated using the Boltzmann equation only when necessary to capture the essential physics.

The other end of the spectrum in plasma models involves taking moments of the Boltzmann equation and averaging over velocity space for each species, which typically assumes local thermodynamic equilibrium to close the equation model. The resulting equations comprise the two-fluid plasma model. The two-fluid equations are then combined to form the magnetohydrodynamic (MHD) model [7]. However, in the process several approximations are made which limit the applicability of the MHD model to low frequency and ignores the electron mass and finite Larmor radius effects. The Larmor radius is the radius of gyration of charged particle in a magnetic field as it undergoes cyclotron motion. The Larmor radius is defined as

$$r_L = \frac{v_T}{\omega_c}, \quad (2)$$

where v_T is the thermal velocity and ω_c is the cyclotron frequency.

The MHD model treats the plasma like a conducting fluid and assigning macroscopic parameters to describe its particle-like interactions. Plasma simulation algorithms based on the MHD model have been very successful in modeling plasma dynamics and other plasma phenomena [8–10]. One successful approach is to formulate an approximate Riemann solver for the MHD model which tracks the wave propagation across the domain [11–13].

A limitation of the MHD model is the treatment the Hall effect and diamagnetic terms. These terms represent the separate motions of the ions and electrons that still preserve the plasma approximation of quasineutrality. The Hall effect and diamagnetic terms also account for ion current and the finite Larmor radius of the plasma constituents. These effects are important in many applications such as space physics, Hall current thrusters and field reversed configurations for magnetic plasma confinement [14,15]. The Hall term is also believed to be important to electrode effects such as anode and cathode fall which greatly affect many directly coupled plasma applications.

In general the Hall terms are difficult to stabilize because they lead to the whistler wave branch of the dispersion relation and the wave velocity increases with frequency. The neglect of electron mass and the displacement current in MHD eliminates the whistler wave resonance at the cyclotron frequency and causes the wave velocity to grow unbounded with frequency. Hall effect physics can be added to the MHD equations and solved. The explicit time step is small and the grid establishes an upper limit on the frequency and, therefore, the maximum wave speed resolved. A large background resistivity can be added to damp fast waves for explicit treatments [16]. The method can fail to converge when the density becomes low and the Hall parameter becomes large [17]. Semi-implicit methods have been developed for incorporating the Hall effect into the MHD model [18]. However, the method is slow to converge for large values of the Hall parameter.

The two-fluid plasma model captures the separate motion of the electrons and ions without the added complexity of the kinetic model. The two-fluid model is derived by taking moments of the Boltzmann equation for each species. The process of taking moments eliminates the velocity space and yields representative fluid variables (density, momentum, energy) for each species. The only approximation made is local thermodynamic equilibrium of each fluid and is, therefore, a generalization of the MHD model. The fundamental variables are generated by taking moments of the distribution function.

This paper describes a new algorithm based on an approximate Riemann solver derived from the two-fluid plasma model.

The evolution of the particle density of the ions and electrons is expressed by continuity equations. The equations are the zeroth moment of the Boltzmann equation

$$\frac{\partial n_i}{\partial t} + \nabla \cdot (n_i \mathbf{v}_i) = 0, \quad (3)$$

$$\frac{\partial n_e}{\partial t} + \nabla \cdot (n_e \mathbf{v}_e) = 0, \quad (4)$$

where n_i , n_e are the ion, electron number densities and \mathbf{v}_i , \mathbf{v}_e are the ion and electron fluid velocities.

The first moment of the Boltzmann equation yields momentum equations for each species

$$n_i m_i \left[\frac{\partial \mathbf{v}_i}{\partial t} + (\mathbf{v}_i \cdot \nabla) \mathbf{v}_i \right] = -\nabla p_i + n_i e (\mathbf{E} + \mathbf{v}_i \times \mathbf{B}) + \mathbf{R}_{ei}, \quad (5)$$

$$n_e m_e \left[\frac{\partial \mathbf{v}_e}{\partial t} + (\mathbf{v}_e \cdot \nabla) \mathbf{v}_e \right] = -\nabla p_e - n_e e (\mathbf{E} + \mathbf{v}_e \times \mathbf{B}) - \mathbf{R}_{ei}, \quad (6)$$

where \mathbf{E} and \mathbf{B} are the electric and magnetic fields, p_i and p_e are the ion and electron partial pressures, and \mathbf{R}_{ei} is the electron to ion momentum transfer vector. For the simulations presented in this paper, the plasma is assumed to be perfectly conducting. Therefore, \mathbf{R}_{ei} is set to zero.

The second moment of the Boltzmann equation yields energy equations for each species

$$\frac{1}{\gamma - 1} n_i \left[\frac{\partial T_i}{\partial t} + (\mathbf{v}_i \cdot \nabla) T_i \right] = -p_i \nabla \cdot \mathbf{v}_i, \quad (7)$$

$$\frac{1}{\gamma - 1} n_e \left[\frac{\partial T_e}{\partial t} + (\mathbf{v}_e \cdot \nabla) T_e \right] = -p_e \nabla \cdot \mathbf{v}_e, \quad (8)$$

where γ is the ratio of specific heats and T_i , T_e are the ion and electron temperatures. An adiabatic equation of state is assumed. The temperatures are related to the partial pressures by $p_\alpha = n_\alpha T_\alpha$ for $\alpha = \{i, e\}$.

2. Development of an approximate Riemann solver

Partial current densities can be defined as

$$\mathbf{j}_i = en_i \mathbf{v}_i \quad \text{and} \quad \mathbf{j}_e = en_e \mathbf{v}_e. \quad (9)$$

where e is the electronic charge. The derivation presented here assumes singly ionized species, $q = e$. (For multiple charged ions, the ion current density definition is modified as $en_i \rightarrow Zen_i$ where Z is the charge state, and the resulting equations are modified accordingly.) Using the partial current densities, the particle continuity equations are then written as

$$\frac{\partial n_i}{\partial t} + \frac{1}{e} \nabla \cdot \mathbf{j}_i = 0 \quad (10)$$

and

$$\frac{\partial n_e}{\partial t} - \frac{1}{e} \nabla \cdot \mathbf{j}_e = 0. \quad (11)$$

Substituting the definitions of partial current densities and using Eqs. (10) and (11), the momentum equations are rewritten in divergence form for the partial current densities with the electromagnetic forces and momentum transfer vector as sources on the right-hand side of the equation.

$$\frac{\partial \mathbf{j}_i}{\partial t} + \nabla \cdot \left(\frac{\mathbf{j}_i \mathbf{j}_i}{en_i} + \frac{e}{m_i} p_i \mathbf{I} \right) = \frac{e^2 n_i}{m_i} \mathbf{E} + \frac{e}{m_i} \mathbf{j}_i \times \mathbf{B} + \frac{e}{m_i} \mathbf{R}_{ei}, \quad (12)$$

$$\frac{\partial \mathbf{j}_e}{\partial t} - \nabla \cdot \left(\frac{\mathbf{j}_e \mathbf{j}_e}{en_e} + \frac{e}{m_e} p_e \mathbf{I} \right) = \frac{e^2 n_e}{m_e} \mathbf{E} - \frac{e}{m_e} \mathbf{j}_e \times \mathbf{B} + \frac{e}{m_e} \mathbf{R}_{ei}. \tag{13}$$

The energy equations can be combined with the corresponding momentum equations to yield energy equations expressed in divergence form for the total energy. The electromagnetic and momentum transfer terms appear as sources on the right-hand side of the equation

$$\frac{\partial \varepsilon_i}{\partial t} + \nabla \cdot \left[(\varepsilon_i + p_i) \frac{\mathbf{j}_i}{en_i} \right] = \mathbf{j}_i \cdot \left(\mathbf{E} + \frac{\mathbf{R}_{ei}}{en_i} \right), \tag{14}$$

$$\frac{\partial \varepsilon_e}{\partial t} - \nabla \cdot \left[(\varepsilon_e + p_e) \frac{\mathbf{j}_e}{en_e} \right] = \mathbf{j}_e \cdot \left(\mathbf{E} + \frac{\mathbf{R}_{ei}}{en_e} \right), \tag{15}$$

where the total energy is defined by

$$\varepsilon_i \equiv \frac{1}{\gamma - 1} n_i T_i + \frac{1}{2} n_i m_i v_i^2 = \frac{1}{\gamma - 1} p_i + \frac{1}{2} n_i m_i v_i^2 \tag{16}$$

and

$$\varepsilon_e = \frac{1}{\gamma - 1} p_e + \frac{1}{2} n_e m_e v_e^2. \tag{17}$$

The two-fluid plasma model does not describe a conservation law except for the relationship between the number densities, current densities, and total energies. The electromagnetic force and ion–electron collision terms introduce sources for the ion and electron momenta and energies.

The two-fluid plasma model is now expressed in divergence form

$$\frac{\partial Q}{\partial t} + \nabla \cdot \mathbf{F} = S, \tag{18}$$

where Q is the vector of conserved fluid variables, \mathbf{F} is the tensor of hyperbolic fluxes ($F\hat{x} + G\hat{y} + H\hat{z}$), and S are the source terms. For the algorithm developed here, the electron to ion momentum transfer is neglected. The vector of conserved fluid variables is

$$Q = [n_i, n_e, j_{ix}, j_{iy}, j_{iz}, j_{ex}, j_{ey}, j_{ez}, \varepsilon_i, \varepsilon_e]^T. \tag{19}$$

The hyperbolic flux tensor in the x direction is

$$F = \begin{bmatrix} \frac{j_{ix}}{e} \\ -\frac{j_{ex}}{e} \\ \frac{j_{ix}^2}{en_i} + \frac{e}{m_i} p_i \\ \frac{j_{ix} j_{iy}}{en_i} \\ \frac{j_{ix} j_{iz}}{en_i} \\ -\frac{j_{ex}^2}{en_e} - \frac{e}{m_e} p_e \\ -\frac{j_{ex} j_{ey}}{en_e} \\ -\frac{j_{ex} j_{ez}}{en_e} \\ (\varepsilon_i + p_i) \frac{j_{ix}}{en_i} \\ -(\varepsilon_e + p_e) \frac{j_{ex}}{en_e} \end{bmatrix}. \tag{20}$$

The flux Jacobian $\partial F/\partial Q$ for the two-fluid equations is constructed in the usual way. The characteristic velocities are calculated to construct the approximate Riemann fluxes.

The eigenvalues of the flux Jacobian give the characteristic velocities

$$\lambda = \left\{ \frac{j_{ix}}{en_i}, \frac{j_{ix}}{en_i} \pm c_{si}, -\frac{j_{ex}}{en_e}, -\frac{j_{ex}}{en_e} \pm c_{se} \right\}, \quad (21)$$

where the ion and electron acoustic speeds are defined as

$$\begin{aligned} c_{si} &= \sqrt{\gamma \frac{T_i}{m_i}} = \sqrt{\gamma \frac{p_i}{m_i n_i}}, \\ c_{se} &= \sqrt{\gamma \frac{T_e}{m_e}} = \sqrt{\gamma \frac{p_e}{m_e n_e}}. \end{aligned} \quad (22)$$

The electron acoustic speed is larger than the ion acoustic speed for the same fluid temperatures due to the large ion to electron mass ratio. The electron acoustic speed can be larger than the Alfvén speed which is a component of the eigenvalues of MHD. The Alfvén speed is defined as

$$v_A = \frac{B}{\sqrt{\mu_0 \rho}}, \quad (23)$$

where B is the magnetic field, ρ is the total mass density, and μ_0 is the permeability of free space ($4\pi \times 10^{-7}$). Therefore, the eigenvalues of the two-fluid model are generally not bounded by the eigenvalues of the MHD model.

The presence of a complete set of real eigenvalues in Eq. (21) proves that the system is hyperbolic. An approximate Riemann solver is appropriate. The eigenvalues for the two-fluid plasma model represent the combination of the drift speeds and thermal speeds for the electrons and ions. For the simulations presented in this paper γ is set to 5/3.

The hyperbolic fluxes of Eq. (18) are discretized using a Roe-type approximate Riemann solver [19]. (Note the source terms of Eq. (18) are treated separately and are discussed later.) In this method the overall solution is built upon the solutions to the Riemann problem defined by the discontinuous jump in the solution between each cell interface. The numerical flux for a first-order accurate (in space) Roe-type solver is written in symmetric form as

$$F_{i+1/2} = \frac{1}{2}(F_{i+1} + F_i) - \frac{1}{2} \sum_k l_k (Q_{i+1} - Q_i) |\lambda_k| r_k, \quad (24)$$

where r_k is the k th right eigenvector, λ_k is the absolute value of the k th eigenvalue, and l_k is the k th left eigenvector, evaluated at the cell interface ($i + 1/2$). The values at the cell interface are obtained either by a simple average of the neighboring cells or a Roe average. Higher-order accuracy is obtained by using a minmod flux limiter in Eq. (24). The algorithm is second-order accurate in regions where the solution is smooth and first-order accurate in the vicinity of large gradients in the solution. The flux calculated as above is normal to the cell interface which is the desired orientation for applying the divergence theorem in a finite volume method.

The eigenvalues of the two-fluid model are well-behaved. There are no zero eigenvalues as there is in the MHD model [20] because the Lorentz force is placed on the right-hand side of Eq. (18) and treated like a force function. The extension to multiple spatial dimensions does not add any complexities not already treated in the one-dimensional approximate Riemann solver. The hyperbolic flux vectors in the y and z directions are similar to the flux vector in the x direction given in Eq. (20). Therefore, the extension to more

than one dimension should be trivial, similar to Euler equations. This is the result of the favorable properties of the two-fluid equations.

The flux tensor of the two-fluid model is a homogeneous function of degree one in Q , like the Euler equations [21]. Additionally, the flux tensor can be written as

$$F \equiv AQ, \tag{25}$$

where A is the flux Jacobian $\partial F/\partial Q$. Therefore, the implicit algorithms which have been used on the Euler equations [22] should work better on the two-fluid model than on the MHD model.

3. Solution of the electromagnetic field equations

The electromagnetic fields influence the motion of the plasma through the Lorentz force which is contained on the right-hand side of Eq. (18). The motion of the plasma influences the evolution of the electromagnetic fields through the redistribution of charge density and current density. Therefore, an accurate solution of the two-fluid plasma model requires the solution of Maxwell’s equation for the electromagnetic fields.

The solution of Maxwell’s equations is performed at each time to obtain the needed coupling between the plasma fluid and the electromagnetic fields. The solution is greatly simplified because the charge density $e(n_i - n_e)$ and current density $(\mathbf{j}_i + \mathbf{j}_e)$ are calculated directly from the two-fluid equations which are then used to solve for the electromagnetic fields

$$\begin{aligned} \frac{\partial \mathbf{B}}{\partial t} &= -\nabla \times \mathbf{E}, \\ \epsilon_o \frac{\partial \mathbf{E}}{\partial t} &= \nabla \times \mathbf{B}/\mu_o + \mathbf{j}_i + \mathbf{j}_e. \end{aligned} \tag{26}$$

The problem is initialized with a solution that satisfies the remaining two Maxwell’s equations which place constraints on the divergence of the electric and magnetic fields.

$$\begin{aligned} \nabla \cdot \mathbf{E} &= e(n_i - n_e)/\epsilon_o, \\ \nabla \cdot \mathbf{B} &= 0. \end{aligned} \tag{27}$$

These divergence constraint equation are not used to calculate the field dynamics of \mathbf{E} and \mathbf{B} . Mathematically, the divergence constraints are preserved by Eq. (26). However, numerical errors can lead to a violation of Eq. (27) and can result in nonphysical results [23]. In multidimensional implementations, methods to prevent the numerical violation of the constraints in Eq. (27) may be necessary. Methods for the solution of Maxwell’s equations have been studied extensively [24–26,28,29]. The methods vary from established finite-difference, time-domain to more advanced integral methods.

For the algorithm described a formulation is developed similar to [26] with the addition of current sources. The time-dependent Maxwell’s equation are written in divergence form as

$$\frac{\partial Q_E}{\partial t} + \nabla \cdot \mathbf{F}_E = S_E, \tag{28}$$

where

$$Q_E = [B_x, B_y, B_z, E_x, E_y, E_z]^T. \tag{29}$$

The electromagnetic field equations are solved with an upwind characteristic-based method. (Note the source terms of Eq. (28) are treated separately and are discussed later.)

Like the two-fluid plasma model, Maxwell's equations do not describe a conservation law except for the relationship between the electric and magnetic fields. The ion and electron momenta (current densities) introduce sources for the electric field.

For one-dimensional electrostatic cases, an electrostatic model is assumed. The electric field is determined by solving Poisson's equation with the charge density and the introduction of the electrostatic potential, ϕ

$$\nabla \cdot \mathbf{E} = -\nabla^2 \phi = e(n_i - n_e)/\epsilon_0. \quad (30)$$

The applied magnetic field is constant.

4. Nondimensionalizing the two-fluid plasma model

The two-fluid plasma model is nondimensionalized by selecting characteristic variables for the length x_0 , plasma size, and velocity v_{Ti} , ion thermal speed, which produces a characteristic time of x_0/v_{Ti} . The partial pressures and total energies are normalized by the ion dynamic pressure $m_i n_0 v_{Ti}^2$ where n_0 is a characteristic number density. The electric field is normalized by the product of the characteristic magnetic field and velocity $B_0 v_{Ti}$.

The nondimensionalized fluid equations are written as

$$\frac{\partial}{\partial t} \begin{bmatrix} n_i \\ n_e \\ \mathbf{j}_i \\ \mathbf{j}_e \\ \varepsilon_i \\ \varepsilon_e \end{bmatrix} + \nabla \cdot \begin{bmatrix} \mathbf{j}_i \\ -\mathbf{j}_e \\ \frac{\mathbf{j}_i \mathbf{j}_i}{n_i} + p_i \mathbf{I} \\ -\frac{\mathbf{j}_e \mathbf{j}_e}{n_e} - \frac{m_e}{m_e} p_e \mathbf{I} \\ (\varepsilon_i + p_i) \frac{\mathbf{j}_i}{n_i} \\ -(\varepsilon_e + p_e) \frac{\mathbf{j}_e}{n_e} \end{bmatrix} = \begin{bmatrix} 0 \\ 0 \\ \frac{1}{\hat{r}_L} (n_i \mathbf{E} + \mathbf{j}_i \times \mathbf{B}) \\ \frac{1}{\hat{r}_L} \frac{m_i}{m_e} (n_e \mathbf{E} - \mathbf{j}_e \times \mathbf{B}) \\ \frac{1}{\hat{r}_L} \mathbf{j}_i \cdot \mathbf{E} \\ \frac{1}{\hat{r}_L} \mathbf{j}_e \cdot \mathbf{E} \end{bmatrix}. \quad (31)$$

The nondimensionalized electromagnetic field equations are written as

$$\frac{\partial}{\partial t} \begin{bmatrix} \mathbf{B} \\ \mathbf{E} \end{bmatrix} + \nabla \times \begin{bmatrix} \mathbf{E} \\ -\hat{c}^2 \mathbf{B} \end{bmatrix} = \begin{bmatrix} 0 \\ -\frac{1}{\hat{\lambda}_D^2 \hat{r}_L} (\mathbf{j}_i + \mathbf{j}_e) \end{bmatrix}. \quad (32)$$

Physically significant similarity parameters appear in the nondimensional equations: ion to electron mass ratio m_i/m_e , normalized speed of light $\hat{c} = c/v_{Ti}$, normalized ion Larmor radius $\hat{r}_L = r_{Li}/x_0$, and normalized the Debye length $\hat{\lambda}_D = \lambda_D/r_L$ where $\lambda_D = \sqrt{\epsilon_0 m v_{Ti}^2 / n e}$. The electron and ion Debye lengths are equal for equal ion and electron temperatures. (For convenience the hat designation is dropped. Normalized variables are used for the remaining sections.) The ion Larmor radius is a measure of importance of two-fluid physics. The electron Larmor radius is related to the ion Larmor radius as $r_{Le} = r_{Li} \sqrt{m_i/m_e}$ for equal ion and electron temperatures.

5. Source term treatment

The source terms appear on the right-hand side of Eqs. (18) and (28). When the source terms are small, they are explicitly incorporated into the complete solution (two-fluid and electromagnetic variables)

$$\frac{Q_i^{n+1} - Q_i^n}{\Delta t} = -\frac{(F_{i+1/2}^n A_{i+1/2} - F_{i-1/2}^n A_{i-1/2})}{V_i} + S_i^n, \quad (33)$$

where Q_i^n is the complete vector of solution variables (two-fluid and electromagnetic) at time step n in cell i , $F_{i+1/2}^n$ is the complete upwind flux vector, S_i^n is the complete vector of the source terms, $A_{i+1/2}$ is the cell interface area, and V_i is the cell volume. An explicit treatment only works when the source terms are small [27]. However, the source terms can become large and make the equations stiff.

The source terms are then treated implicitly. The homogeneous fluxes are calculated for the electron and ion fluids with the approximate Riemann solver described previously, and the upwind method is used to calculate the homogeneous fluxes for Maxwell’s equations. The source terms for all of the equations are then solved self-consistently with an implicit treatment to alleviate the stiffness of the problem. The full discretized equation with implicit source terms is

$$\frac{Q_i^{n+1} - Q_i^n}{\Delta t} = - \frac{(F_{i+1/2}^n A_{i+1/2} - F_{i-1/2}^n A_{i-1/2})}{V_i} + S_i^{n+1}. \quad (34)$$

The source terms are expanded in a Taylor series to first-order and the resulting Newton iteration is written as

$$\left[\frac{1}{\Delta t} - \left(\frac{\partial S}{\partial Q} \right)_i^k \right] \Delta Q = - \frac{Q_i^k - Q_i^n}{\Delta t} - \frac{(F_{i+1/2}^n A_{i+1/2} - F_{i-1/2}^n A_{i-1/2})}{V_i} + S_i^k, \quad (35)$$

where $\Delta Q = Q_i^{n+1} - Q_i^k$ and k is the iteration variable.

After the numerical fluxes F^n are calculated explicitly as described, the source terms are solved implicitly. Within each iteration the linear system, Eq. (35), is solved using a symmetric Gauss–Seidel method. Two or three iterations are typically used. The source flux Jacobian in Eq. (35) is recalculated and Q is updated after each iteration until $|\Delta Q|$ approaches zero. Ten Newton iterations are typically sufficient to converge. It is important to note that $(\partial S / \partial Q)_i^k$ is local, and S does not depend on the value of Q in adjacent cells. Therefore, the computational work required to solve Eq. (35) increases linearly with the number of cells in the domain, even when the algorithm is extended to three dimensions.

The solution is advanced in time with first-order accuracy. Higher-order accurate time differencing can be used at the expense of additional flow solutions from previous times. The implicit treatment is stable for time steps less than the minimum of ω_{pe}^{-1} and $\Delta x/c$. The implicit method is fast and for simulations where both the explicit and implicit schemes produce stable solutions for the same time step, the explicit method is 30% faster than the implicit method. The explicit method becomes less appealing for stiff source terms which occur for normalized Larmor radii less than 1 in the electromagnetic shock problem. In these cases, the time step for the explicit method must be reduced to obtain a stable solution, and the implicit method is more than 10 times faster than the explicit method.

6. Validation tests

The approximate Riemann solver developed in this work is validated against known analytical results. The solver is used to simulate the coplanar Riemann problem to test for proper wave capturing behavior, Langmuir oscillations to test the electric field component in the Lorentz force, and the electromagnetic plasma shock to illustrate the ability of the algorithm to capture the MHD shock in the limit of $r_L \rightarrow 0$, the gas dynamic shock in the limit of $r_L \rightarrow \infty$, and two-fluid (Hall effect) physics for intermediate values. The MHD model assumes $r_L = 0$ where the electron and ion fluids are tightly coupled to the magnetic field. The plasma completely decouples from the magnetic field when $r_L = \infty$.

6.1. Electrostatic tests

The coplanar Riemann (or shock tube) problem is used to test the fundamental behavior of the approximate Riemann solver. As expected from an approximate Riemann solver, wave structures are well captured. The behavior is best seen when the effect of the electromagnetic fields is eliminated by artificially setting the electron and ion charge to zero and reducing the effect of the large mass difference by setting the electron mass to 20% of the ion mass, $m_e = 0.2m_i$. The electron and ion fluids then decouple and behave as independent fluids. Results are shown in Figs. 1 and 2. The coplanar Riemann problem is initiated with normalized electron and ion number densities of 4.0 on the right-hand side of the domain and 1.0 on the left hand side of the domain. The normalized electron and ion temperatures are initialized at a uniform value of 10. The domain is discretized into 256 volumes. Fig. 1 shows the evolution of the electron and ion number densities after 150 time steps. The characteristic shock wave, contact discontinuity, and rarefaction wave are clearly evident in both the electron and ion fluid. The more massive ion fluid has slower characteristic wave speeds. The sound speed varies like the square root of the mass. Fig. 2 shows the evolution of the electron and ion current densities in the longitudinal direction after 150 time steps. When the effect of the electromagnetic fields is included, the faster electron fluid is slowed by the slower, massive ion fluid. The number density jumps are altered as the flow is limited by ambipolar motion.

The ability to capture gas dynamic waves as shown in the coplanar Riemann problem is expected from an approximate Riemann solver. The approximate Riemann solver for two-fluid plasma model must also capture plasma wave behavior. This ability is demonstrated by simulating Langmuir plasma oscillations. Langmuir plasma oscillations are the plasmas response to charge concentrations created by perturbations in the plasma. In one dimension, the equation of motion for electrons reduces to a second-order differential equation for the particle position

$$\frac{d^2x}{dt^2} = -\frac{n_e e^2}{m_e \epsilon_0} x = -\omega_{pe}^2 x, \quad (36)$$

where ω_{pe} is the electron plasma frequency. If the plasma pressure is negligible and the fluid velocity is sufficiently small, the two-fluid plasma model can produce Langmuir plasma oscillations. A sinusoidal perturbation is initialized to the electron fluid.

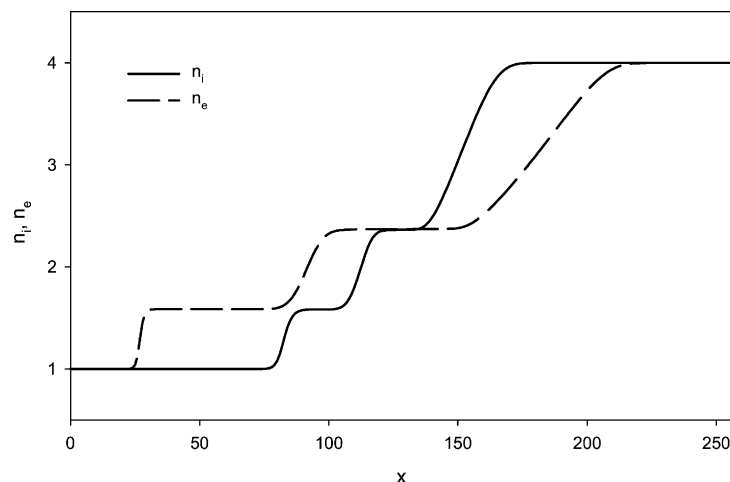


Fig. 1. Electron and ion number densities for a shock tube simulation. The shock wave, contact discontinuity, and rarefaction wave can be seen in each fluid.

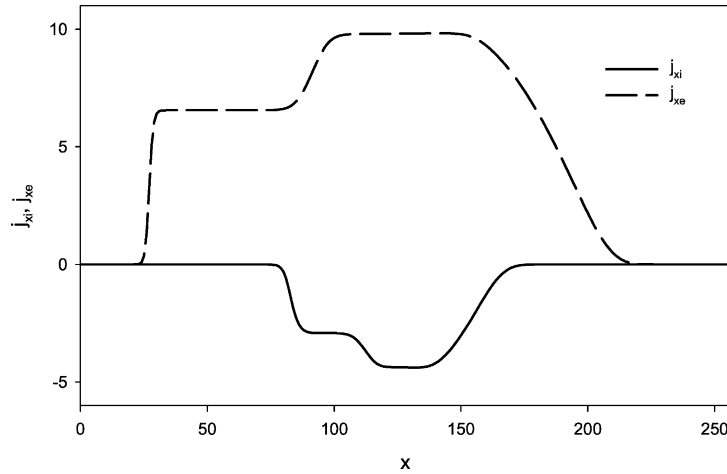


Fig. 2. Electron and ion current densities for a shock tube simulation.

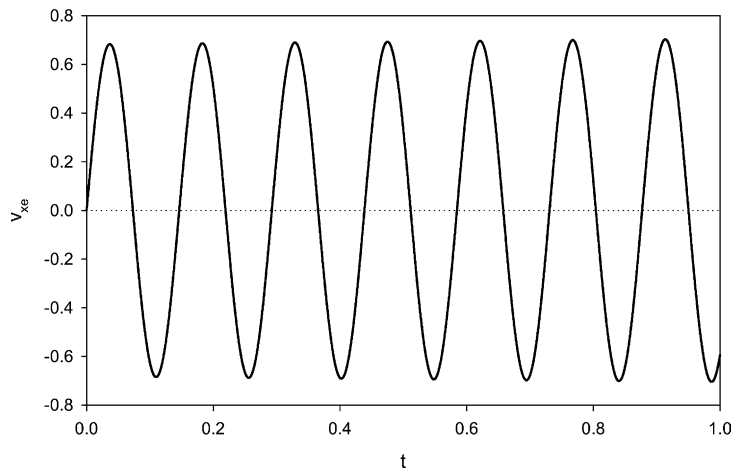


Fig. 3. Time history of the electron velocity measured at a fixed spatial location demonstrating Langmuir plasma oscillations.

The results are shown in Figs. 3 and 4. The theoretical plasma frequency as determined from the previous equation is $\omega_{pe} = 0.1466$ for the normalized plasma parameters used in the simulation. The numerically generated frequency of $\omega_{pe} = 0.1462$ agrees with the theoretical value with an error of 0.27%.

6.2. Electromagnetic plasma shock

The two-fluid algorithm is applied to the electromagnetic plasma shock problem which is a generalization of the MHD shock problem published in [11]. The shock problem is a good test of the two-fluid algorithm’s ability to model asymptotic MHD-like behavior and to demonstrate the departure of the solution when two-fluid effects are included. MHD problems are characterized by strong coupling of the plasma fluid and the magnetic field. The two-fluid model allows the ion and electron fluid to have a more physically correct coupling to the magnetic field as characterized by the ion and electron Larmor radii.

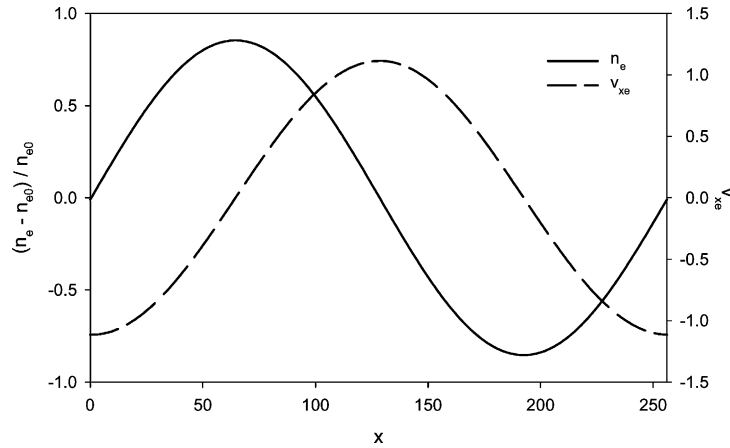


Fig. 4. Spatial structure of the electron density and velocity at single time during a Langmuir plasma oscillation simulation.

Mathematically, the electromagnetic plasma shock problem is an initial boundary value problem in which there is initially a discontinuity in the data such that the left half of the domain is at one state and the right half of the domain is at another state. As the solution evolves in time, characteristic waves form and travel at speeds related to the wave speeds of the system.

The MHD shock problem forms waves that travel at the characteristic wave speeds of the MHD model. For reference, the MHD wave speeds are given by

$$\lambda_{\text{MHD}} = \{v_x, v_x \pm v_{\text{fast}}, v_x \pm v_{\text{slow}}, v_x \pm v_{Ax}\}, \quad (37)$$

where v_{fast} and v_{slow} are the fast and slow magnetosonic speeds, and v_{Ax} is the Alfvén speed based on the x component of the magnetic field which are defined as

$$v_{\text{fast}}^2 = \frac{1}{2} \left[c_s^2 + v_A^2 + \sqrt{(c_s^2 + v_A^2)^2 - 4c_s^2 v_{Ax}^2} \right], \quad (38)$$

$$v_{\text{slow}}^2 = \frac{1}{2} \left[c_s^2 + v_A^2 - \sqrt{(c_s^2 + v_A^2)^2 - 4c_s^2 v_{Ax}^2} \right], \quad (39)$$

$$v_{Ax}^2 = \frac{B_x^2}{\mu_0 \rho}. \quad (40)$$

The acoustic speed c_s is given by

$$c_s^2 = \frac{\gamma p}{\rho}, \quad (41)$$

where p is the total pressure, ρ is the total mass density, v_x is the mass-averaged, single-fluid velocity in the x direction, and μ_0 is the permeability of free space ($4\pi \times 10^{-7}$).

The problem is initialized with a uniform longitudinal magnetic field B_x and discontinuities in the densities, the pressures, and the transverse magnetic field B_y . The initial values are chosen to allow a direct comparison with the MHD shock problem published in [11]. The initial left plasma state is specified as

$$\begin{bmatrix} \rho \\ v_x \\ v_y \\ v_z \\ p \\ B_x \\ B_y \\ B_z \end{bmatrix}_{\text{left}} = \begin{bmatrix} 1.0 \\ 0 \\ 0 \\ 0 \\ 1.0 \\ 0.75 \\ 1.0 \\ 0 \end{bmatrix}. \tag{42}$$

The initial right plasma state is specified as

$$\begin{bmatrix} \rho \\ v_x \\ v_y \\ v_z \\ p \\ B_x \\ B_y \\ B_z \end{bmatrix}_{\text{right}} = \begin{bmatrix} 0.125 \\ 0 \\ 0 \\ 0 \\ 0.1 \\ 0.75 \\ -1.0 \\ 0 \end{bmatrix}. \tag{43}$$

The solution to the MHD shock problem is shown in Fig. 5. The wave features of the MHD solution are identified with labels in the figure. From left to right in the figure, a fast rarefaction wave (FR) and a slow compound wave (SC) move to the left, and a contact discontinuity (CD), a slow shock (SS), and a fast rarefaction wave (FR) move to the right. The slow compound wave is composed of a slow shock and an attached slow rarefaction wave [11]. The gas dynamic solution shows a rarefaction wave, a contact discontinuity, and a shock.

The two-fluid variables can be written in terms of species mass densities, species velocities, and species pressures. The MHD variables are related to these two-fluid variables as

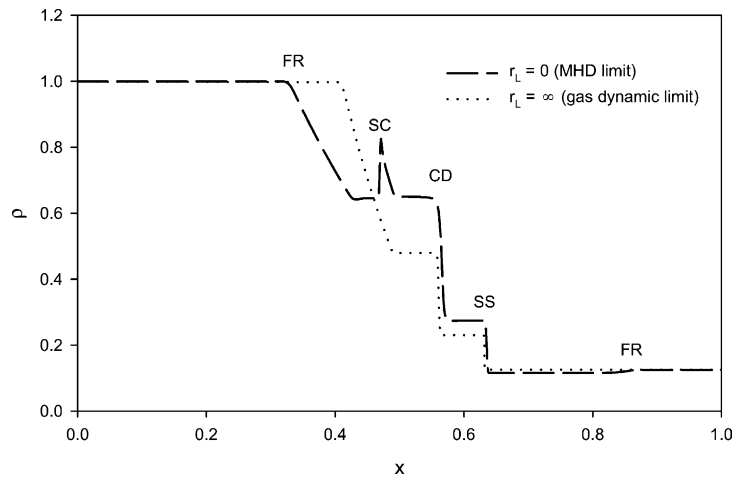


Fig. 5. The two asymptotic solutions of the electromagnetic plasma shock problem showing the total mass density for the MHD limit $r_L = 0$ and for the gas dynamic limit $r_L = \infty$. Labels identify wave features of the MHD solution shows, from left to right, a fast rarefaction wave (FR), a slow compound wave (SC), a contact discontinuity (CD), a slow shock (SS), and a fast rarefaction wave (FR). The gas dynamic solution shows a rarefaction wave, a contact discontinuity, and a shock. The two-fluid solution with $r_L = 100$ is indistinguishable from the gas dynamic solution.

$$\begin{bmatrix} \rho \\ v_x \\ v_y \\ v_z \\ p \\ B_x \\ B_y \\ B_z \end{bmatrix} = \lim_{\frac{m_e}{m_i} \rightarrow 0} \begin{bmatrix} \frac{\rho_i + \rho_e}{\rho_i v_{ix} + \rho_e v_{ix}} \\ \frac{\rho_i + \rho_e}{\rho_i v_{iy} + \rho_e v_{iy}} \\ \frac{\rho_i + \rho_e}{\rho_i v_{iz} + \rho_e v_{iz}} \\ p_i + p_e \\ B_x \\ B_y \\ B_z \end{bmatrix} = \begin{bmatrix} \rho_i \\ v_{ix} \\ v_{iy} \\ v_{iz} \\ p_i + p_e \\ B_x \\ B_y \\ B_z \end{bmatrix}. \tag{44}$$

In the MHD model it is assumed that $n_i = n_e$ and $p_i = p_e$.

Equivalent initial conditions for the electromagnetic plasma shock using two-fluid variables are

$$\begin{bmatrix} \rho_e \\ v_{ex} \\ v_{ey} \\ v_{ez} \\ p_e \\ \rho_i \\ v_{ix} \\ v_{iy} \\ v_{iz} \\ p_i \\ B_x \\ B_y \\ B_z \\ E_x \\ E_y \\ E_z \end{bmatrix}_{\text{left}} = \begin{bmatrix} 1.0 \frac{m_e}{m_i} \\ 0 \\ 0 \\ 0 \\ 0.5 \\ 1.0 \\ 0 \\ 0 \\ 0 \\ 0.5 \\ 0.75 \\ 1.0 \\ 0 \\ 0 \\ 0 \\ 0 \end{bmatrix} \tag{45}$$

and

$$\begin{bmatrix} \rho_e \\ v_{ex} \\ v_{ey} \\ v_{ez} \\ p_e \\ \rho_i \\ v_{ix} \\ v_{iy} \\ v_{iz} \\ p_i \\ B_x \\ B_y \\ B_z \\ E_x \\ E_y \\ E_z \end{bmatrix}_{\text{right}} = \begin{bmatrix} 0.125 \frac{m_e}{m_i} \\ 0 \\ 0 \\ 0 \\ 0.05 \\ 0.125 \\ 0 \\ 0 \\ 0 \\ 0.05 \\ 0.75 \\ -1.0 \\ 0 \\ 0 \\ 0 \\ 0 \end{bmatrix}. \tag{46}$$

The initial total mass density differs slightly from the MHD density since the electrons have a finite mass in the two-fluid model.

For the electromagnetic plasma shock simulations presented here, the ion to electron mass ratio is set to 1836 (∞ in MHD), and the ionic charge state is set to unity as in MHD. The normalized Debye length is set to 0.01, and the normalized speed of light is set to 100. The ion Larmor radius is varied. The values normalized by the length of the domain are $r_L = 100, 10, 1, 0.1, 0.01, 0.003$. Total mass density plots reveal the structure of the shock solution and allows comparison to MHD and gas dynamic results. The solutions presented have been converged by increasing the grid resolution until the solution does not change appreciably.

The simulation results of the density plots at the same time are presented in Figs. 6–10. The two asymptotic solutions (the MHD solution which assumes $r_L = 0$ and the gas dynamic solution which assumes $r_L = \infty$) are shown in Fig. 5 and in each figure showing the two-fluid solutions for comparison.

When the ion and electron Larmor radii are much larger than the domain, the plasma is essentially decoupled from the magnetic field and the plasma species are decoupled from each other. The discontinuity in the transverse magnetic field B_y expands quickly leaving the ion fluid essentially stationary. Without the attachment of a finite mass fluid the magnetic field propagates as a smooth continuous function, and the initial discontinuity vanishes. Since the electron mass is much less than the ion mass, the electron fluid also expands before the ion fluid moves significantly. The ion fluid behaves like a neutral gas. For the case with $r_L = 100$, the two-fluid solution is indistinguishable from the gas dynamic solution since the ion fluid distribution governs the total mass density distribution, $\rho = \rho_i + \rho_e m_e/m_i \approx \rho_i$.

When the Larmor radius is decreased to $r_L = 10$, the solution departs slightly from the gas dynamic solution, as seen in Fig. 6. However, the magnetic field, electron fluid, and ion fluid are still mostly decoupled similar to the case of $r_L = 100$. The solution is only slightly modified from the $r_L = 100$ case. The motion of the magnetic field, electron fluid, and ion fluid is qualitatively similar as before. The electrostatic force causes the “gas dynamic” shock in the ion fluid to travel at a slightly higher speed than the larger Larmor radius simulation. The position of the shock is at $x = 0.64$.

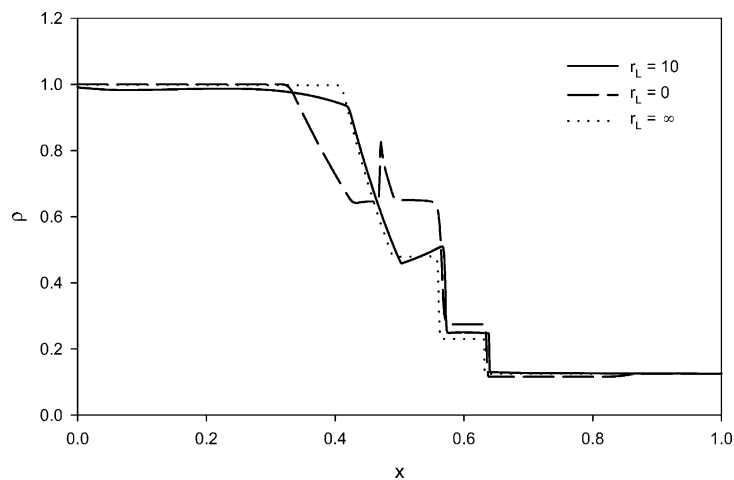


Fig. 6. Two-fluid solution of the electromagnetic plasma shock problem for $r_L = 10$ showing the total mass density. The two asymptotic solutions of the gas dynamic limit $r_L = \infty$ and the MHD limit $r_L = 0$ are also shown for comparison. The electrostatic force between the electron and ion fluids cause the solution to depart from the gas dynamic solution. The “gas dynamic” shock in the ion fluid is at $x = 0.64$.

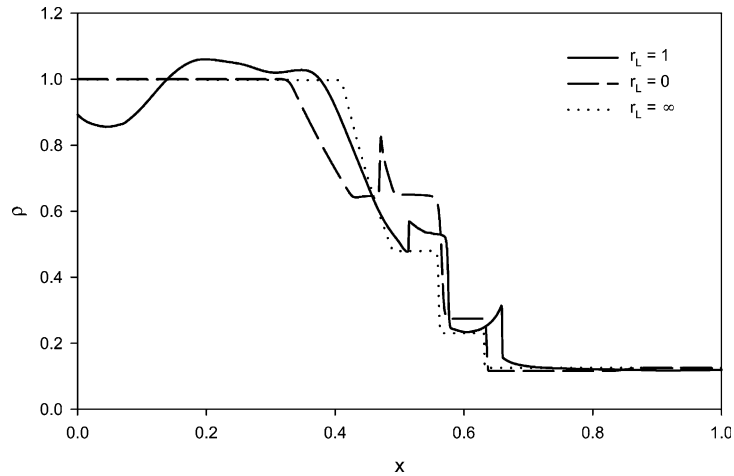


Fig. 7. Two-fluid solution of the electromagnetic plasma shock problem for $r_L = 1$ showing the total mass density. The two asymptotic solutions of the gas dynamic limit $r_L = \infty$ and the MHD limit $r_L = 0$ are also shown for comparison. Note that the two-fluid solution contains wave-like structure that propagates faster than the MHD waves. The “gas dynamic” shock in the ion fluid is at $x = 0.66$.

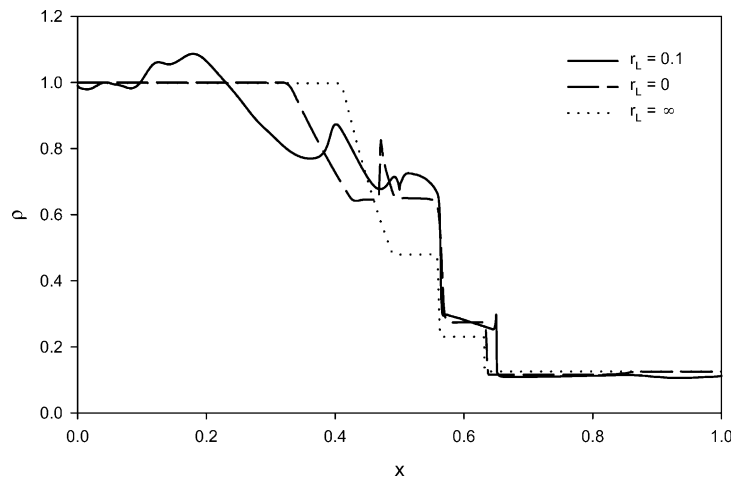


Fig. 8. Two-fluid solution of the electromagnetic plasma shock problem for $r_L = 0.1$ showing the total mass density. The two asymptotic solutions of the gas dynamic limit $r_L = \infty$ and the MHD limit $r_L = 0$ are also shown for comparison. Note that the two-fluid wave-like structure propagates slower than for $r_L = 1$ but still faster than the MHD waves.

Fig. 7 shows the solution for a Larmor radius of $r_L = 1$. The solution contains wave-like structures that propagate faster than the MHD waves. As is shown later, the fast waves are electron plasma waves, such as L mode and R mode which includes the whistler wave, which couple to the ion fluid. At this Larmor radius value the electron fluid is coupled to the magnetic field, and the electron fluid responds to the magnetic field as the magnetic field propagates away from the initial discontinuity. The electrostatic force between the electron and ion fluids generates an effect on the ion fluid as the electron fluid reacts to the magnetic field expansion. The speed of the ion fluid “gas dynamic” shock has increased due to the increased coupling with the electron fluid and the corresponding electrostatic force. The position of the shock has moved to $x = 0.66$ from $x = 0.64$.

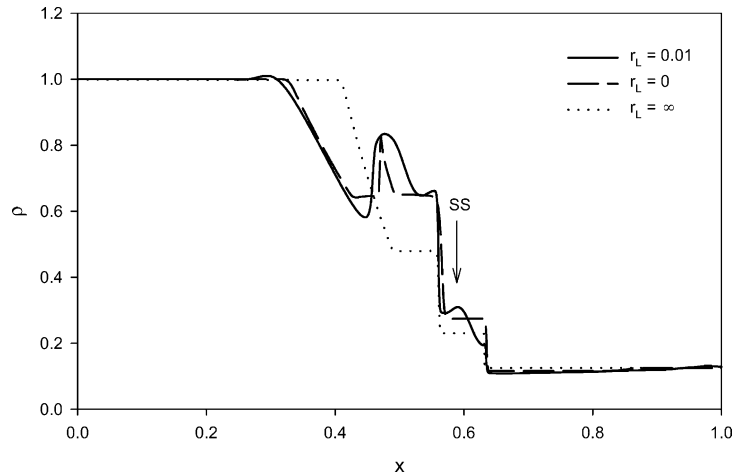


Fig. 9. Two-fluid solution of the electromagnetic plasma shock problem for $r_L = 0.01$ showing the total mass density. The two asymptotic solutions of the gas dynamic limit $r_L = \infty$ and the MHD limit $r_L = 0$ are also shown for comparison. Note that fast waves of the two-fluid solution have slowed and the solution is beginning to approach the MHD solution. The MHD slow shock is forming as a smooth bump at approximately $x = 0.59$.

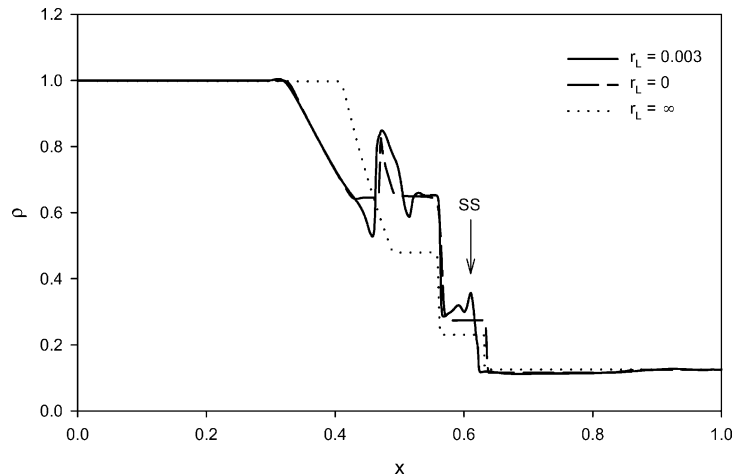


Fig. 10. Two-fluid solution of the electromagnetic plasma shock problem for $r_L = 0.003$ showing the total mass density. The two asymptotic solutions of the gas dynamic limit $r_L = \infty$ and the MHD limit $r_L = 0$ are also shown for comparison. Note that the two-fluid solution is approaching the MHD solution. The slow shock in the two-fluid solution is well-formed as a sharp discontinuity at $x = 0.62$ and is approaching the location in the MHD solution at $x = 0.635$.

As the Larmor radius is decreased further to $r_L = 0.1$, the solution begins to develop some of the general features of the MHD solution. The solution can be seen in Fig. 8. The wave-like structures that propagate faster than the MHD waves are still present. At this Larmor radius value the electron fluid is coupled to the magnetic field. The ion fluid is electrostatically coupled to the electron fluid and loosely coupled to the magnetic field. The massive ion fluid alters the speed and shape of the propagating magnetic field. The position of the “gas dynamic” shock has decreased as the propagation speed of the electron fluid and magnetic field have decreased.

Fig. 9 shows the solution for a Larmor radius of $r_L = 0.01$. The fast waves have slowed and the solution begins to approach the MHD solution. Features of the MHD solution are beginning to form. The formation of the slow shock of the MHD solution is visible in Fig. 9 as a smooth bump at approximately $x = 0.59$. Note the collocation of the “gas dynamic” shock with the MHD slow shock is coincidental. The MHD slow shock is identified by a jump in the magnetic field and in the density.

When the Larmor radius is decreased to $r_L = 0.003$, the solution approaches the MHD solution. See Fig. 10. The fastest moving waves in the positive and negative directions correspond to the rarefaction waves of the MHD solution. The two-fluid solution clearly shows a structure similar in shape and location as the slow compound wave of the MHD solution. In particular, the steeper leading edge of the structure corresponds to the slow shock component of the slow compound wave. The solution also shows the position of a well-formed slow shock that is approaching the location of the MHD slow shock at $x = 0.635$. The position of the two-fluid slow shock has moved to $x = 0.62$.

The simulations show as the Larmor radius decreases, the two-fluid solution approaches the MHD solution. The transition from gas dynamic shock to MHD shock is a smooth transition that has not been previously published. The general case of intermediate values of Larmor radius shows the importance of two-fluid effects as waves propagate away from the discontinuity faster than the waves predicted by the MHD model.

The character of the fast moving waves is studied. The electromagnetic plasma shock simulation is repeated for the case of $r_L = 0.1$. The amplitudes of the discontinuities are decreased to 10^{-6} to keep the waves in the linear regime. The initial conditions on the left and right side of the domain are set to

$$\begin{bmatrix} \rho_e \\ v_{e_x} \\ v_{e_y} \\ v_{e_z} \\ p_e \\ \rho_i \\ v_{i_x} \\ v_{i_y} \\ v_{i_z} \\ p_i \\ B_x \\ B_y \\ B_z \\ E_x \\ E_y \\ E_z \end{bmatrix}_{\text{left}} = \begin{bmatrix} 1.0 \frac{m_e}{m_i} \\ 0 \\ 0 \\ 0 \\ 0.5 \\ 1.0 \\ 0 \\ 0 \\ 0 \\ 0.5 \\ 0.75 \\ 10^{-6} \\ 0 \\ 0 \\ 0 \\ 0 \end{bmatrix} \quad \text{and} \quad \begin{bmatrix} \rho_e \\ v_{e_x} \\ v_{e_y} \\ v_{e_z} \\ p_e \\ \rho_i \\ v_{i_x} \\ v_{i_y} \\ v_{i_z} \\ p_i \\ B_x \\ B_y \\ B_z \\ E_x \\ E_y \\ E_z \end{bmatrix}_{\text{right}} = \begin{bmatrix} (1 - 10^{-6}) \frac{m_e}{m_i} \\ 0 \\ 0 \\ 0 \\ 0.5(1 - 10^{-6}) \\ 1 - 10^{-6} \\ 0 \\ 0 \\ 0 \\ 0.5(1 - 10^{-6}) \\ 0.75 \\ -10^{-6} \\ 0 \\ 0 \\ 0 \\ 0 \end{bmatrix}. \tag{47}$$

The time-dependent numerical results are Fourier analyzed to transform from time and physical space to frequency and wave number space. A contour plot of the results is shown in Fig. 11. The contours of the logarithm of the signal amplitude show the presence of plasma waves structures. Plasma waves propagating parallel to a magnetic field should produce left and right circularly polarized waves described by the dispersion relation

$$\frac{c^2 k^2}{\omega^2} = 1 - \frac{\omega_{pe}^2}{\omega(\omega \pm \omega_{ce})}. \tag{48}$$

The + sign in the denominator gives the left circularly polarized wave (L mode), and the – sign in the denominator gives the right circularly polarized wave (R mode). The R mode generates two branches in the

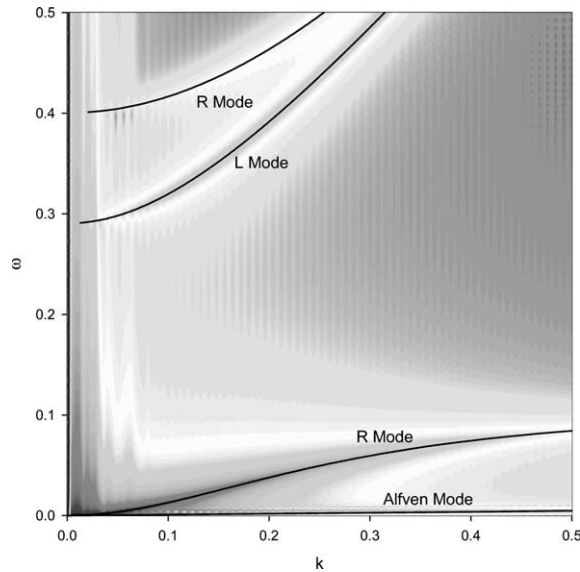


Fig. 11. Fourier analysis of the numerical results for a small amplitude electromagnetic plasma shock compared to the analytical dispersion relations for plasma waves for $r_L = 0.1$. The analytical dispersion relations for the L mode, R mode, and Alfvén mode waves are shown. The low frequency portion of the lower branch of the R mode is the whistler wave. The agreement of the numerical and analytical results supports the physical basis for the fast waves in the two-fluid solutions.

dispersion relation. The group velocity increases with frequency for the low frequency portion of the lower branch of the R mode, which produces the whistler wave. Analytical dispersion relations for the L mode, R mode, and Alfvén mode waves are plotted in Fig. 11 for comparison using the same flow parameters. The agreement of the numerical and analytical results supports the physical basis for the fast waves in the two-fluid solutions.

7. Discussion

An algorithm is developed for the simulation of plasma dynamics using the two-fluid plasma model. The algorithm uses an approximate Riemann solver to compute the fluxes of the electron and ion fluids at the computational cell interfaces and an upwind characteristic-based solver to compute the electromagnetic fields. The source terms couple the fluids and fields and are treated implicitly to relax the stiffness.

The two-fluid plasma model is more general than the standard MHD model that is often used for plasma dynamic simulations. In particular, it can model plasmas where ion and electron motions separate while still preserving the plasma approximation of quasineutrality. In the MHD model this phenomena is responsible for the Hall effect and diamagnetic current which includes ion current and the finite Larmor radius of the plasma constituents.

The approximate Riemann solver algorithm presented is capable of simulating plasmas with the two-fluid plasma model. The algorithm accurately models the coplanar Riemann problem and Langmuir plasma oscillations. The algorithm is applied to the electromagnetic shock problem that has been simulated with the MHD plasma model. The algorithm is able to produce the correct asymptotic results when the Larmor radius is large (gas dynamic limit) and when the Larmor radius is small (MHD limit). Furthermore, when the Larmor radius is an intermediate value, the shock solution shows fast moving plasma waves.

These fast moving waves which are not included in the MHD model can be important for many applications.

The extension of the algorithm to multiple dimensions can be accomplished by calculating the fluxes at each cell interface in the same manner. The divergence theorem can then be applied.

References

- [1] J.S. Chang, G. Cooper, *J. Comput. Phys.* 6 (1970) 1.
- [2] A.R. Bell, *Astrophys. Space Sci.* 256 (1998) 13.
- [3] C.Z. Cheng, G. Knorr, *J. Comput. Phys.* 22 (1976) 330.
- [4] H. Ruhl, P. Mulser, *Phys. Lett. A* 205 (1995) 388.
- [5] L. Chacón, D.C. Barnes, D.A. Knoll, G.H. Miley, *J. Comput. Phys.* 157 (2000) 618.
- [6] L. Chacón, D.C. Barnes, D.A. Knoll, G.H. Miley, *J. Comput. Phys.* 157 (2000) 654.
- [7] J.P. Freidberg, *Rev. Mod. Phys.* 54 (1982) 801.
- [8] I.R. Lindemuth, *J. Comput. Phys.* 18 (1975) 119.
- [9] R.E. Peterkin Jr., M.H. Frese, C.R. Sovinec, *J. Comput. Phys.* 140 (1998) 148.
- [10] A.H. Glasser, C.R. Sovinec, R.A. Nebel, T.A. Gianakon, S.J. Plimpton, M.S. Chu, D.D. Schnack, *Plasma Phys. Control. Fusion* 41 (1999) A747.
- [11] M. Brio, C.C. Wu, *J. Comput. Phys.* 75 (1988) 400.
- [12] A.L. Zachery, P. Colella, *J. Comput. Phys.* 99 (1992) 341.
- [13] O.S. Jones, U. Shumlak, D.S. Eberhardt, *J. Comput. Phys.* 130 (1997) 231.
- [14] A. Ishida, H. Momota, L.C. Steinhauer, *Phys. Fluids* 31 (1988) 3024.
- [15] N. Iwasawa, A. Ishida, L.C. Steinhauer, *Phys. Plasmas* 7 (2000) 931.
- [16] A. Otto, *J. Geophys. Res.* 106 (A3) (2001) 3751.
- [17] M. Hesse, J. Birn, M. Kuznetsova, *J. Geophys. Res.* 106 (A3) (2001) 3721.
- [18] D. Harned, Z. Mikic, *J. Comput. Phys.* 83 (1989) 1.
- [19] P.L. Roe, *J. Comput. Phys.* 43 (1981) 357.
- [20] D.L. DeZeeuw, T.I. Gombosi, C.P.T. Groth, K.G. Powell, Q.F. Stout, *IEEE Trans. Plasma Sci.* 28 (2000) 1956.
- [21] J.L. Steger, R.F. Warming, *J. Comput. Phys.* 40 (1981) 263.
- [22] S. Yoon, A. Jameson, *AIAA J.* 26 (1988) 1025.
- [23] J.U. Brackbill, D.C. Barnes, *J. Comput. Phys.* 35 (1980) 426.
- [24] K.S. Yee, *IEEE Trans. Antennas Propag.* 14 (1966) 302.
- [25] R.L. Morse, C.W. Nielson, *Phys. Fluids* 14 (1971) 830.
- [26] J.S. Shang, R.M. Fithen, *J. Comput. Phys.* 125 (1996) 378.
- [27] R. Schneider, C.D. Munz, *Int. J. Numer. Model.* 8 (1995) 399.
- [28] A.R. Bretones, A. Monorchio, G. Manara, R. Gomez-Martin, R. Mitra, *Electron. Lett.* 36 (2000) 506.
- [29] V. Jandhyala, E. Micheilssen, S. Balasubramaniam, W.C. Chew, *IEEE Trans. Geosci. Remote Sensing* 36 (1998) 738.